

Applied-field magnetic structure and spectroscopy shifts of the effective spin- $\frac{1}{2}$, XY-like magnet Li_2CoCl_4

Zachary W. Riedel,^{1,2} Mykhaylo Ozerov,³ Stuart Calder,⁴ and Daniel P. Shoemaker^{1,2,*}

¹*Department of Materials Science and Engineering,
University of Illinois Urbana-Champaign, Urbana, IL 61801, USA*

²*Materials Research Laboratory, University of Illinois Urbana-Champaign, Urbana, IL 61801, USA*

³*National High Magnetic Field Laboratory, Florida State University, Tallahassee, FL 32310, USA*

⁴*Neutron Scattering Division, Oak Ridge National Laboratory, Oak Ridge, TN 37831, USA*

Insulators containing chains of magnetic transition metal cations provide platforms for probing spin- $\frac{1}{2}$ dynamics and quantum critical behavior. Li_2CoCl_4 contains edge-sharing CoCl_6 octahedra that form chains along the crystallographic c axis and orders antiferromagnetically at zero field, but questions remain about its applied-field magnetic structure and the Co^{2+} spin state. Here, we show with neutron diffraction on a polycrystalline sample how the anti-aligned chains of cobalt moments undergo a spin-flop transition to a field-aligned ferromagnetic state above 1.6 T. Further, using magnetic resonance absorption measurements and paramagnetic spin models, we reveal the strongly anisotropic nature of the Co^{2+} ion's XY-like magnetic behavior ($g_{\parallel} = 2.77$ and $g_{\perp} = 5.23$) and its $J = \frac{1}{2}$ ground state. We, therefore, supply the magnetic structures and anisotropic description needed to explore the dynamics of the field-driven magnetic phases, laying the foundation for further experimental and theoretical studies.

I. INTRODUCTION

Low-dimensional magnetic materials frequently provide access to quantum behavior, and scattering studies on unexplored, spin- $\frac{1}{2}$ materials are critical for validating low-dimensional magnetism models that may be extended to higher-dimensional systems [1]. Of note here, several compounds with chains of edge-sharing $\text{Co}^{2+}X_6$ polyhedra have exhibited quantum criticality [2–4]. We identified Li_2CoCl_4 as a low-dimensional magnetism candidate with a dimensional analysis toolkit [5]. Li_2CoCl_4 contains Co^{2+} octahedrally coordinated to Cl^- , forming edge-sharing polyhedral chains along the crystallographic c axis.

The ionic conductivity of Li_2MCl_4 compounds has been studied extensively [6–15], but magnetic property measurements have been limited to susceptibility data used to determine the spin states of Mn^{2+} and Fe^{2+} in cubic Li_2MnCl_4 [16] and Li_2FeCl_4 [17]. For orthorhombic Li_2CoCl_4 , high temperature susceptibility data indicate spin- $\frac{3}{2}$ (high-spin) behavior with significant unquenched orbital angular momentum, and heat capacity data point to a ground-state Kramers doublet ($J = \frac{1}{2}$) dominating low-temperature behavior [18]. Other high-spin Co^{2+} chlorides exhibit similar effective spin- $\frac{1}{2}$ behavior, leading to fruitful studies of spin excitations and quantum criticality [3, 19–22]. Therefore, we were encouraged to map the magnetic phases of Li_2CoCl_4 .

At zero field, Li_2CoCl_4 orders antiferromagnetically with P_Cbam magnetic space group symmetry. The Co^{2+} magnetic moments align within edge-sharing CoCl_6 chains and anti-align between nearest neighbor chains. The magnetic susceptibility and heat capacity shift with

increasing field, leading to three proposed magnetic phase regions separated by transitions near 1.6 T and 3.5 T at 2 K [18]. The magnetic structures of the applied-field regions are unknown. The low-field region is antiferromagnetic, likely similar to the zero-field magnetic ordering. The intermediate-field region may be ferrimagnetic, with chain rotations reminiscent of the structurally similar compound $\text{CoCl}_2 \cdot 2\text{H}_2\text{O}$ [23, 24], though the data were also consistent with a spin-flop reorientation. Finally, in the high-field region, not sharply delineated from the intermediate-field one, the Li_2CoCl_4 moment chains are likely field-aligned, with no well-defined Curie temperature in the magnetic susceptibility.

Here, we use polycrystalline Li_2CoCl_4 to identify the applied-field regions' magnetic structures with neutron diffraction, particularly that of the previously ambiguous intermediate-field region. Additionally, we extract several parameters from applied-field infrared spectroscopy data, such as the anisotropic g -factors, to discuss the role of spin-orbit coupling and anisotropic interactions on the magnetic properties of Li_2CoCl_4 .

II. MATERIALS AND METHODS

We prepared polycrystalline Li_2CoCl_4 as previously described [18]. We ground LiCl (99.9%, Alfa Aesar) and CoCl_2 (99.7%, Alfa Aesar) under argon, sealed the mixture under vacuum, heated it to 550°C at 10°C/min, held for 12 h, then cooled to room temperature at 10°C/min. We ensured that the highly hygroscopic LiCl and Li_2CoCl_4 powders remained under inert atmospheres during synthesis and characterization.

We collected neutron diffraction data on the HB-2A beamline at the High Flux Isotope Reactor at Oak Ridge National Laboratory. To avoid grain reorientation under applied field, we pressed pellets of Li_2CoCl_4 for the

* dpshoema@illinois.edu

diffraction experiment. Under argon, we pressed 1.5 g of powder into around 30 1/8" diameter pellets. We then sealed the pellets under vacuum, transported them to ORNL, and loaded them under helium into a 6 mm diameter vanadium canister. The top of the canister was packed with aluminum foil before being hermetically sealed.

We collected constant wavelength (2.41 Å) neutron diffraction data using a Ge(113) monochromator with the instrument in an open-open-12' pre-mono, pre-sample, pre-detector collimation. The sample was cooled to base temperature (1.5–1.6 K) under zero field before collecting powder scans that covered 2θ angles from 6.025° to 127.525° in 0.05° steps with $\mu_0 H = 0, 0.8, 1.5, 2.5, 3.5, 4.5,$ and 5.5 T. We also collected a zero-field scan at 20 K (above the ordering temperature). The cryomagnet contributed a significant reflection at $2\theta = 19.9^\circ$. Sweeping scans monitored select magnetic reflections with increasing field or temperature, also after zero-field cooling. To analyze the neutron diffraction data, we used GSAS-II [25] in combination with the Bilbao Crystallographic Server's *K-SUBGROUPSMAG* program [26], generating magnetic structure images with VESTA [27].

We performed magneto-infrared measurements at the infrared (IR) spectroscopy facility at the National High Field Magnetic Laboratory with a 17.5 T vertical-bore superconducting magnet coupled to a Bruker Vertex 80v FTIR spectrometer. In an argon glovebox, a 3–5 mg polycrystalline sample was bonded with n-eicosane and loaded between two polypropylene layers to protect it from oxygen and moisture. We placed the sample in a Voigt geometry so that the incoming IR light was perpendicular to the magnetic field. A composite Si bolometer (IR Labs) collected the transmitted IR light with a spectral range of $10\text{--}1100\text{ cm}^{-1}$ ($0.3\text{--}33\text{ THz}$) and a resolution of 0.3 cm^{-1} (9 GHz). Additionally, we placed a low-pass THz filter (QMC Instruments) with a 120 cm^{-1} cutoff frequency in front of the sample to increase sensitivity in the far-IR (FIR) range and to minimize radiative heating. IR data were collected near 5 K.

To isolate the magnetic resonance absorption, the spectra were divided by the average spectrum for all magnetic fields. Such normalized spectra are only sensitive to intensity shifts due to magnetic field and eliminate contributions from nonmagnetic vibrational absorption and instrument features. Our data analysis utilized the EPR analysis package EASYSPIN [28].

III. RESULTS

A. Zero- and low-field magnetic structures

We first confirmed that the zero-field magnetic structure matches that determined previously. The data refines well to the antiferromagnetic structure with P_Cbam (BNS no. 55.363) magnetic space group symmetry (see supplemental material [29]). For the magnetic space

group P_Cbam , only reflections where $h + k \neq 2n$ are allowed, whereas the nuclear $Cmmm$ space group only allows reflections where $h + k = 2n$, making it simple to identify the magnetic ordering reflections. The magnetic structure is commensurate, with the propagation vector $\mathbf{k} = (1,0,0)$. The magnetic moments are aligned within the Co^{2+} chains and anti-aligned between nearest neighboring chains along the nuclear cell's *ab*-plane diagonal. The refined moment is $2.10(3)\ \mu_B$. The 20 K, zero-field data in the paramagnetic region is included in the supplemental material for comparison [29].

We noticed several low-intensity impurity peaks at $2\theta = 17.0, 30.4, 46.6, 53.0,$ and 68.5° ($Q = 0.77, 1.37, 2.06, 2.32,$ and $2.93\ \text{\AA}^{-1}$), the largest impurity peak being only 0.8% the intensity of the largest Li_2CoCl_4 peak. The $Q = 0.77\ \text{\AA}^{-1}$ peak also appears in X-ray diffraction data after exposing a sample to air for 15–30 s before sealing it under vacuum [29]. The reflections do not change with temperature, indicating they are nonmagnetic, and they do not influence data analysis.

Prior magnetic susceptibility and heat capacity data indicated that the low-field magnetic structure (< 1.6 T) matches the zero-field structure. At 0.8 T, we observe the same magnetic reflections as in the zero-field case, associated with a loss of *C*-centering, but with slightly decreased intensity. Refinements give an unconstrained magnetic moment of $2.02(3)\ \mu_B$ (Fig. 1), indicating some magnetic intensity may become paramagnetic background, though restricting the moment to $2.10\ \mu_B$ gives a nearly identical fit. With the field increased to 1.5 T, just below the 1.6 T transition to the intermediate-field phase, we can again refine the data well to the P_Cbam structure with a constrained $2.10\ \mu_B$ moment or a refined moment of $1.96(3)\ \mu_B$. See the supplemental material [29] for the 1.5 T refinement.

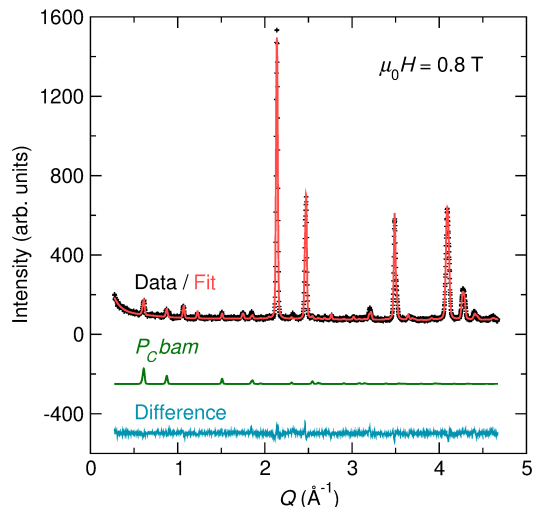


FIG. 1. The neutron powder diffraction data collected at 1.5 K and 0.8 T refine well to the antiferromagnetic magnetic phase also observed at zero field with a $2.02(3)\ \mu_B$ moment along the *c* axis for Co^{2+} . The refined lattice parameters are $a = 7.1711(3)$, $b = 10.2393(5)$, and $c = 3.6111(2)\ \text{\AA}$.

B. Field-induced moment rotation

Between the 1.5 T and 2.5 T scans, the $h + k \neq 2n$ antiferromagnetic structure reflections, e.g. (010), (100), and (120), lose significant intensity while the $h + k = 2n$ reflections allowed by the C -centered nuclear cell, e.g. (110) and (020), gain intensity. The intensity shifts indicate a spin reorientation to a $\mathbf{k} = \mathbf{0}$ magnetic structure. Unlike for $\text{CoCl}_2 \cdot 2\text{H}_2\text{O}$ [23, 24], we do not observe new peaks associated with a ferrimagnetic phase. Instead, a spin-flop transition begins to align the chains of Co^{2+} magnetic moments.

Because the measured sample is polycrystalline, the magnetic field is not along a specific crystallographic direction and the spin-flop transition is spread out, leading to a slow evolution within the sample and a mixture of magnetic phases. Therefore, the best refinement models above 1.6 T involve both the antiferromagnetic P_Cbam magnetic phase and a ferromagnetic $\mathbf{k} = \mathbf{0}$ structure with moments along the crystallographic c axis. The moment is constrained to be equal in the two magnetic phases when both are refined. The full Q range refinements for the 2.5, 3.5, 4.5, and 5.5 T data are shown in Fig. S5 [29]. Fig. 2 shows both magnetic unit cells along with the nuclear cell. The ferromagnetic structure has $Cm'm'm$ symmetry (BNS no. 65.485). This maximal magnetic space group only allows a Co^{2+} moment along c .

Several factors oppose modeling the magnetic structure with the other maximal groups $Cmm'm'$ (moments along a only) and $Cm'mm'$ (moments along b only). First, the increasing intensity on the (020) reflection violates the $Cm'mm'$ systematic absence of $(0k0)$ reflections. Second, at higher fields, the significant increase in intensity on the (110) reflection (Fig. 3), though allowed for both the $Cm'm'm$ and $Cmm'm'$ symmetries, suggests a preferred moment alignment along c . Only the moment component within the (110) plane, and thus perpendicular to the corresponding scattering vector, will contribute to the magnetic intensity. For moments along c , this component equals the magnitude of the total moment for the $Cm'm'm$ symmetry structure but is less than the magnitude of the total moment for the $Cmm'm'$ symmetry structure. Consequently, fitting with $Cmm'm'$ does not account for the full (110) reflection intensity increase (Fig. 3). Third, a model with moments along c fits nicely with the previously established zero-field structure and the proposed spin-flop transition. At 5.5 T, a majority of the moments are likely aligned along c .

Additionally, commensurate magnetic structures that allow for canting do not improve the magnetic peak fits. For example, the $C2'/m'$ space group symmetry (BNS no. 12.62) is the highest symmetry $\mathbf{k} = \mathbf{0}$ magnetic space group possible for Li_2CoCl_4 that allows for moment components along a and c . Refinements to the high-field data using $C2'/m'$ ($M_a = 1.5(2) \mu_B$, $M_c = 1.7(1) \mu_B$) or $Cm'm'm$ symmetry gave a similar fit [29]. Therefore, we tentatively retain the simpler model of Co^{2+} moments flipping along c with increasing field.

TABLE I. Rietveld refinement results for base temperature, constant applied field scans are listed. Scans below 1.6 T only include the antiferromagnetic P_Cbam phase, while those above 1.6 T also include the ferromagnetic $Cm'm'm$ phase. The Co^{2+} magnetic moment is along the c axis in both cases.

Field (T)	Magnetic Phase (% P_Cbam - % $Cm'm'm$)	Refined Moment (μ_B)
0	100 - 0	2.10(3)
0.8	100 - 0	2.02(3)
1.5	100 - 0	1.96(3)
2.5	81(6) - 19(6)	1.59(7)
3.5	42(3) - 58(3)	1.76(6)
4.5	17(2) - 83(2)	2.07(6)
5.5	10(2) - 90(2)	2.05(6)

The refinement results for the base temperature scans with the P_Cbam and $Cm'm'm$ magnetic space group structures are recorded in Table I. Refinements to the 2.5 and 5.5 T data, corresponding to the previously described intermediate-field and high-field regions, are in Fig. 4, which highlights the changing magnetic intensity contributions of the antiferromagnetic and ferromagnetic phases. At 2.5 and 3.5 T, the refined magnetic moment dips significantly. The shift corresponds with the antiferromagnetic phase (010) reflection's drop with increasing field (Fig. 5), with the shift to a steeper slope in the magnetization curve [18], and with emerging $Cm'm'm$ phase magnetic intensity. If we constrain the moment for every field to the zero-field value of $2.10 \mu_B$, the 2.5 T refinement shows the largest change [29] while the other results are qualitatively identical.

While tracking the (010) reflection intensity with increasing field, we additionally captured changes in several lower intensity reflections with the other diffractometer detectors: the antiferromagnetic (100) reflection and the nuclear/ferromagnetic (131) reflection. Both show the same general trend of increasing ferromagnetic intensity and decreasing antiferromagnetic intensity above 1.5–1.6 T [29]. Additionally, we monitored the ferromagnetic (110) reflection's changes with increasing temperature in the high-field region at 5.6 T (Fig. 6). Up to 20 K, we do not observe a sharp drop or leveling off of the intensity but rather a nearly linear decrease in reflection intensity. Similarly, the magnetic susceptibility at high field, even up to 7 T [29], does not show the typical sharp rise of a paramagnetic to ferromagnetic transition, suggesting that the high-field magnetic ordering is driven by field overcoming the material's interchain antiferromagnetic exchange interactions instead of by dominant interchain ferromagnetic exchange interactions.

C. IR spectroscopy in an applied magnetic field

The normalized FIR magnetic resonance absorption contains a broad continuum and a narrow peak (Fig. 7a). The broad continuum shows the strongly anisotropic re-

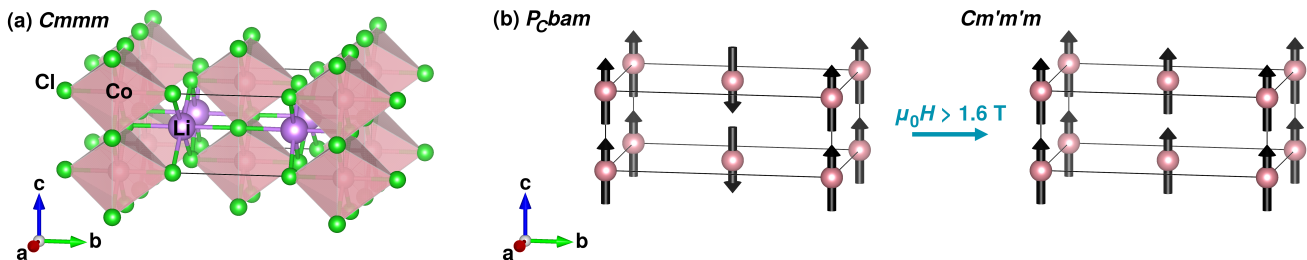


FIG. 2. The nuclear and magnetic cells of Li_2CoCl_4 are identified by their space groups. (a) The nuclear (and paramagnetic) unit cell contains chains of edge-sharing Co-Cl octahedra along c connected by chains of Li-Cl octahedra along a . (b) At zero field and below ~ 7 K, Co^{2+} chains are ferromagnetic with antiferromagnetic interchain interactions, breaking the cell's C -centering. For applied fields above 1.5–1.6 T, ferromagnetic ordering emerges as the antiferromagnetic interactions are overcome.

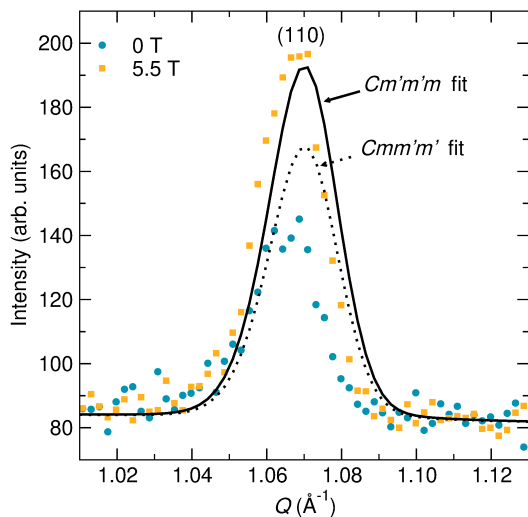


FIG. 3. The magnetic intensity gained by the (110) peak with increasing field is better fit using a ferromagnetic phase with moments along the c axis ($Cm'm'm$) than with moments along the a axis ($Cmm'm'$).

sponse of the Li_2CoCl_4 sample, which contains crystallites randomly oriented relative to the magnetic field. At high fields, where Zeeman effects dominate, we extracted anisotropic g -factors of $g_{\parallel} = 2.77$ and $g_{\perp} = 5.23$, where \parallel and \perp are relative to the compressed CoCl_6 axis (crystallographic b axis at base temperature). A narrow absorption peak is also observed in the middle of the continuum that is consistent with a g -factor of 4.16. The corresponding resonance lines confine the magnetic absorption spectrum for a free cobalt ion, but the experimental data diverge from the lines below 10 T where exchange interactions produce collective spin excitations.

Approaching zero field, the magnetic anisotropy decreases, and the continuum collapses to the same shape for each crystallite. The magnetic field where the absorption transitions between continuum and gapped behavior, notably, matches that of the transition between regions dominated by field-aligned moments and spin-flop

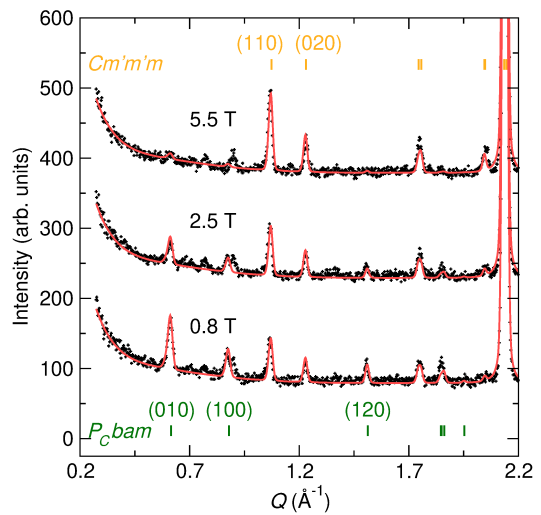


FIG. 4. Neutron powder diffraction data from the three regions (antiferromagnetic, spin-flop, ferromagnetic) are shown with several reflections labeled to highlight the phase contribution changes with increasing field. All unfit peaks are from the instrument/impurity features mentioned in the main text.

behavior. At zero field, we attribute the strong peak at 11.6 cm^{-1} and the weaker satellite at 17.2 cm^{-1} (Fig. 7c) to spin gaps in the collective excitations of Li_2CoCl_4 . Because we are unaware of structural analogues to Li_2CoCl_4 with which we could create a magnetically dilute system, we were unable to probe the $< 10 \text{ cm}^{-1}$ region with electron paramagnetic resonance measurements.

IV. DISCUSSION

A. Magnetic structure evolution

The zero-field magnetic ordering determined by neutron diffraction data agrees with data collected previously [18]. Below T_N and at zero field, Co^{2+} moments with magnitude $2.10(3) \mu_B$ are aligned within chains

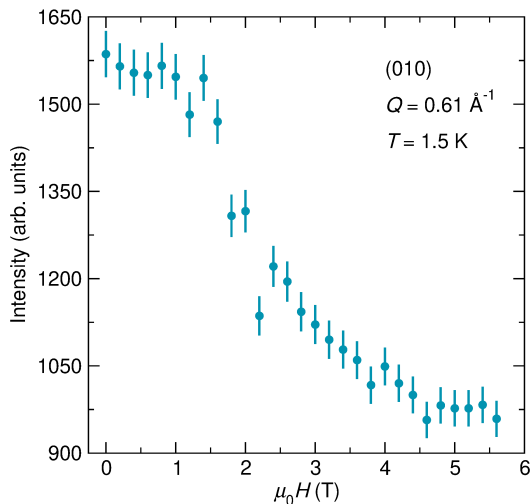


FIG. 5. With increasing field, the antiferromagnetic (010) reflection intensity is constant before decreasing with the emergence of the ferromagnetic phase near 1.5–1.6 T. Above 4.5 T, the intensity levels off as the ferromagnetic phase dominates.

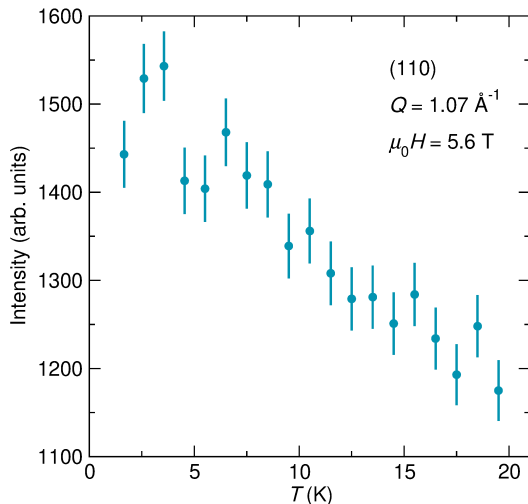


FIG. 6. With increasing temperature, the nuclear and ferromagnetic (110) reflection intensity drops linearly and does not show a critical point below 19.5 K.

while antiferromagnetic interactions between chains lead to a cusp in the susceptibility and a negative Curie-Weiss temperature. Though the moment in this study is slightly lower than the previously refined value $2.19(4) \mu_B$, the refinement standard errors are likely underestimated. Since we were able to produce a closer fit to peak intensities in this work, especially nuclear intensity, we will use $2.10 \mu_B$ here.

With increasing field, the field-aligned ferromagnetic $Cm'm'm$ phase emerges. The notable appearance of the ferromagnetic phase near 1.6 T in neutron data matches the slope increase of the magnetization, the susceptibility's leveling off below the critical temperature, and the emergence of a hump in the magnetic heat capacity

alongside a sharper peak. The suppression of the heat capacity antiferromagnetic transition peak along with the emergence of the heat capacity hump follows from the reduction of antiferromagnetic regions and the progressive aligning of chains in newly formed ferromagnetic regions in the polycrystalline samples. Since the 2.5 T, 1.5 K neutron diffraction data captures the region of greatest competition between the antiferromagnetic and ferromagnetic interactions, which reduces the refined magnetic moment, it is the only pattern where constraining the moment to the zero-field value of $2.10 \mu_B$ significantly alters the refinement. At higher fields where the ferromagnetic phase dominates, the refined moment returns, within error, to its zero-field value.

Unlike in $\text{CoCl}_2 \cdot 2\text{H}_2\text{O}$, the emergence of a field-driven ferromagnetic phase is not preceded by a collective reorientation of only one-third of the chains. The difference in behavior may be due to the distance between anti-aligned chains in the zero-field structures (5.6 \AA for $\text{CoCl}_2 \cdot 2\text{H}_2\text{O}$ and 6.2 \AA for Li_2CoCl_4), producing a weaker next-nearest-neighbor (antiferromagnetic) exchange interaction in Li_2CoCl_4 , and thus a lower barrier to overcoming the interaction with applied field. DFT results from the previous work also indicated that for a 3.5 K experimental cell, the $Cm'm'm$ moment arrangement was higher in energy than the P_Cbam moment arrangement by only 0.62 meV/atom [18]. Trivially, for an isolated $2.10 \mu_B$ moment along c paired with an anti-aligned 1.6 T field, the energy gain for flipping the moment is 0.39 meV ($2\mu_{\text{Co}}B$). For 5.5 T, the energy gain would be 1.34 meV . The proposed magnetic structure changes are, therefore, energetically reasonable. At 5.5 T, almost no antiferromagnetic reflection intensity remains.

B. Paramagnetic free-ion model

Spin exchange interactions clearly influence the properties of Li_2CoCl_4 at the magnetic fields probed with neutron diffraction. The IR data, though, includes information not only in those field regions, but also at fields significantly above the moment saturation field, where the Zeeman energy dominates antiferromagnetic spin-spin interactions and the magnetic anisotropy energy [30]. We can, therefore, approximate the spectroscopic behavior of Li_2CoCl_4 with a paramagnetic spin model at high fields. The paramagnetic resonance energy equals $g\mu_B B$ with a g -factor range of $[g_{\parallel}, g_{\perp}]$ depending on the crystal-lite orientation relative to the magnetic field. We estimated the g -factors by fitting high-field data slices with line shape simulations of a spin- $\frac{1}{2}$ system. For the fits (e.g. Fig. 7b), we used the linewidth of the strongest zero-field peak (Fig. 7c). Introducing additional in-plane anisotropy overparameterized the model, with slight variations in the value ($\Delta g = \pm 0.1$) having no significant impact on subsequent analysis.

Also of note is the narrow absorption peak within the broader continuum of Fig. 7a at high fields. The line

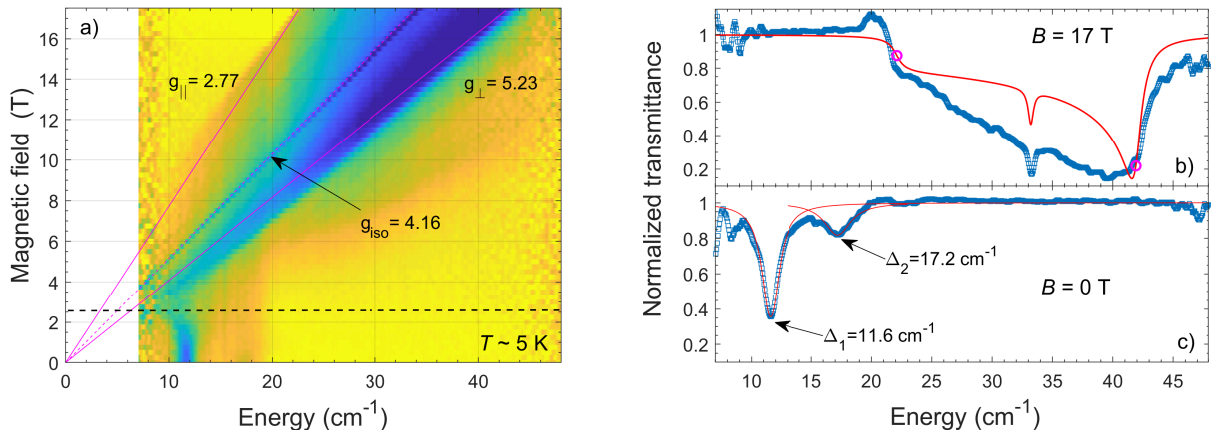


FIG. 7. (a) The normalized transmission heat map at 5 K is shown with magenta lines representing (an)isotropic g -factors for a paramagnetic $S = \frac{1}{2}$ system and a black dashed line at the saturation field from magnetization data in Ref. [18]. (b) A heat map slice at 17 T (blue dots) shows agreement with a simulated powder spectrum (red line) with 98% of the intensity from a paramagnetic $S = \frac{1}{2}$ site with an anisotropic g -factor (g_{\perp} and g_{\parallel} , magenta points) and 2% from a site with an isotropic g -factor of 4.16. (c) Lorentzian peak fits (red curves) to a heat map slice at zero field demonstrate the nearly two-fold linewidth difference in the spin-gap peaks.

shape is well-fit by a single peak, indicating an isotropic g -factor. Therefore, the peak may originate from a Co^{2+} site with minimal axial distortion. A similar peak was observed in the X-band EPR spectrum of LiCoO_2 and was ascribed to a high-spin Co^{2+} site on the surface of polycrystalline sample [31, 32]. Powder spectrum simulations with an effective spin- $\frac{1}{2}$ model that consider a mixture of isotropic (surface) and anisotropic (bulk) Co^{2+} sites (Fig. 7b) indicate that 2% of the Co^{2+} sites are isotropic. We will regard the fraction as a small paramagnetic impurity and will ignore it while interpreting other magnetic property measurements of powder samples.

Still, for the extracted g -factors, we need to justify an effective spin- $\frac{1}{2}$ model for high-spin (spin- $\frac{3}{2}$) Co^{2+} in Li_2CoCl_4 , with the only previous evidence of applicability being entropy changes extracted from the magnetic heat capacity [18]. Observed g -factor values are well-studied for high-spin Co^{2+} with a local octahedral environment [33–36]. Under a cubic field, the ground state of Co^{2+} is a ${}^4T_{1g}({}^4F)$ orbital triplet with $L_{\text{eff}} = 1$ and $S = \frac{3}{2}$, and the following Hamiltonian describes the low-energy diagram [35]:

$$H = -\lambda\mathbf{L}\cdot\boldsymbol{\alpha}\cdot\mathbf{S} + \Delta(L_z^2 - \frac{2}{3}) + \mu_B\mathbf{B}(g_e\mathbf{S} - \hat{\alpha}\mathbf{L}) \quad (1)$$

λ is the spin-orbit coupling constant, Δ is the crystal field energy due to axial distortion, \mathbf{B} is the magnetic field vector, g_e is the free-electron g -factor, and α is the orbital reduction factor. Without axial distortion or a magnetic field, the first-order spin-orbit coupling splits the twelve-fold degenerate ${}^4T_{1g}$ state, making a $J = \frac{1}{2}$ doublet the lowest energy level. The ground state doublet produces effective spin- $\frac{1}{2}$ behavior with an isotropic g -factor of $g_0 = (10 + 2\alpha)/3$. The covalency of metal-ligand

bonds or admixture of higher-energy orbital states, e.g. ${}^4T_{1g}({}^4P)$, can produce α values from 1 to 1.5, giving isotropic g -factors between 4 and 4.33 [37].

Axial distortion of the ideal octahedral environment of the Co^{2+} ion further splits the J manifold, leading to a different g value when a magnetic field is applied along or perpendicular to the distortion axis. For distortion values (Δ) small relative to the spin-orbit exchange constant ($\lambda\alpha$), the g -factor anisotropy is approximately [37]:

$$\begin{aligned} g_{\perp} &= g_0 + \frac{8\Delta}{27\lambda\alpha}(\alpha + 2) \\ g_{\parallel} &= g_0 - 2\frac{8\Delta}{27\lambda\alpha}(\alpha + 2) \end{aligned} \quad (2)$$

The average g -factor in this case remains independent of the distortion effects since $g_{\text{avg}} = (2g_{\perp} + g_{\parallel})/3 = g_0$. For our data, g_{avg} is 4.41, which agrees well with an isotropic g -value of 4.33 corresponding to high-spin Co^{2+} ion in the weak crystal field limit ($\alpha = 1.5$). This spectroscopic determination of the high average g -factor also corroborates the neutron diffraction moment, which we would expect to equal $g_{\text{avg}}J\mu_B = 2.2\mu_B$. Therefore, the observed g -factors for Li_2CoCl_4 confirm a $J = \frac{1}{2}$ ground state, allowing for the modeling of the material as an effective spin- $\frac{1}{2}$ system at low temperatures.

Solving the free Co^{2+} ion Hamiltonian (Eq. 1) further allows us to probe the interplay between the spin-orbit exchange constant and crystal field axial distortion in Li_2CoCl_4 . Using the EASYPIN package [28], we tuned the axial distortion and calculated the resulting g -factor dependence, assuming an isotropic orbital reduction factor (Fig. 8a). The best match to the experimental g -factor values is $\Delta/(\lambda\alpha) = 2$ with an adjusted α parameter

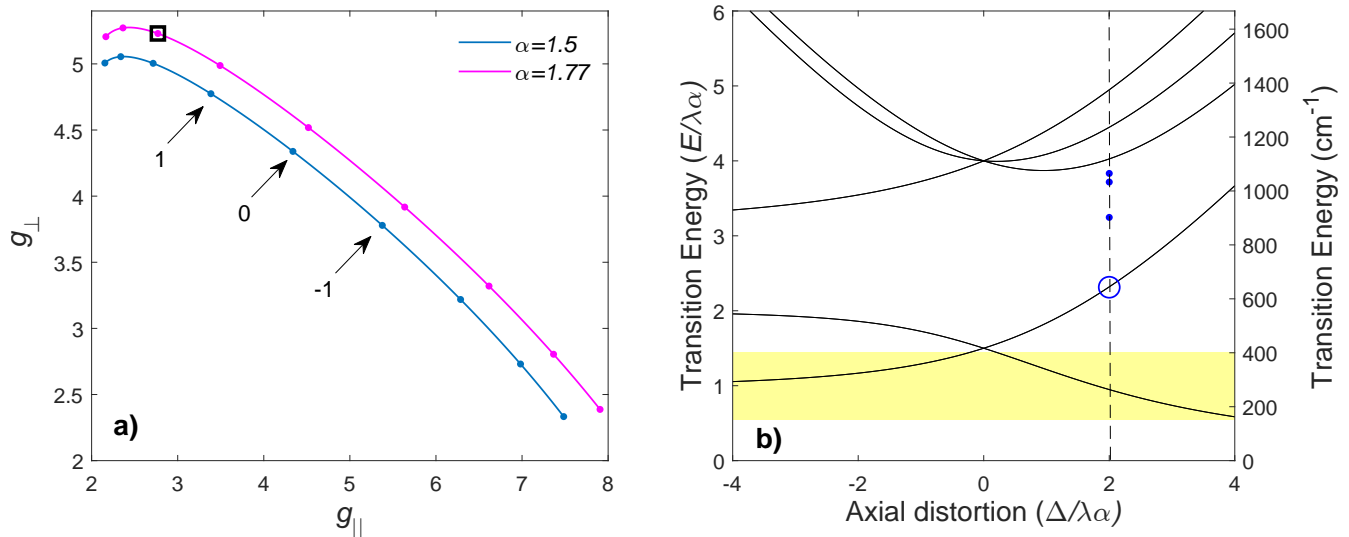


FIG. 8. (a) Curves show the change in g -factor anisotropy with axial distortion for orbital reduction factors of 1.5 and 1.77 with points indicating integer values of $\Delta/(\lambda\alpha)$. (b) The spectrum for a free Co^{2+} ion is calculated for $\alpha = 1.77$ as a function of $E/(\lambda\alpha)$ (left-hand axis) or assuming $\lambda = 157 \text{ cm}^{-1}$ (right-hand axis). The dashed line matches the distortion derived from the experimental g -factor anisotropy. The shaded area is opaque to FIR radiation, preventing observation of transitions to the first excited Kramers doublet.

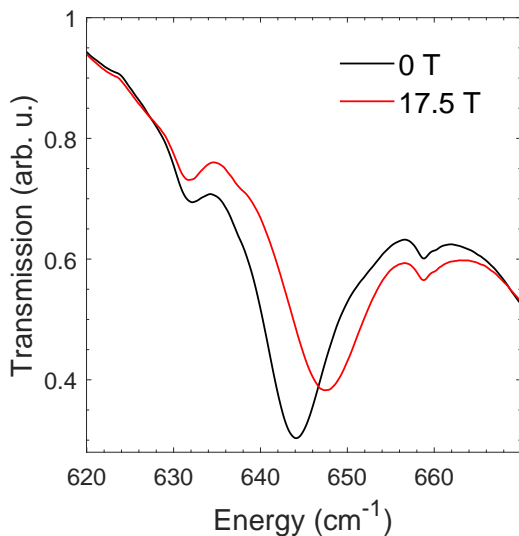


FIG. 9. The transmission spectra of the Li_2CoCl_4 powder sample measured at 0 and 17.5 T. The absorption peak at 644 cm^{-1} shifts under high magnetic fields, while the small peaks, likely associated with phonons, remain at the same position.

of 1.77, which is close to the weak crystal field case of 1.5. Such an increase in the reduction factor is reasonably similar to a previous analysis of cobalt salts [33] and demonstrates the deficiencies of neglecting the magnetic coupling between neighboring Co^{2+} ions [37].

Besides its influence on the g -factor, the octahedral

distortion also substantially modifies the energy levels of the ${}^4T_{1g}$ state, causing a splitting into six Kramers doublets. The excitation energy, i.e. the energy difference between the higher-energy Kramers doublets and the ground state, is calculated and shown in Fig. 8b in dimensionless units of the spin-orbit exchange constant. An applied magnetic field further splits the Kramers doublets, allowing us to distinguish the corresponding spectroscopic peaks from other spectroscopic features in the transmission spectrum. Indeed, a pronounced absorption peak at 644 cm^{-1} reveals a noticeable shift and broadening under applied magnetic fields (Fig. 9). We attribute this energy to a transition from the ground state to the second excited Kramers doublet, highlighted by a blue circle in Fig. 8b. Using the previously estimated values of α and Δ , this energy yields a spin-orbit coupling constant of $\lambda = 157 \text{ cm}^{-1}$, consistent with the 178 cm^{-1} value for a free Co^{2+} ion [33]. The transition to the first excited state, however, is not observed in the transmission spectrum because of a strong absorption band between 200 and 400 cm^{-1} . Nevertheless, additional field-dependent spectral features (blue dots in Fig. 8b) were observed at higher energies (Fig. S8 [29]) and are likely associated with the remaining inter-Kramers doublet transitions. While the free-ion model does not provide a complete quantitative description of the IR transmission spectrum, it qualitatively approximates the underlying physics of the Co^{2+} ion in Li_2CoCl_4 .

C. Spin gaps below the saturation field

Within the free-ion model framework, the observed 11.6 cm^{-1} gap could be interpreted as the zero-field energy of a $S = \frac{3}{2}$ system. Exploring this possibility, we found moderate agreement between the experimental absorption and a $S = \frac{3}{2}$ Hamiltonian with a single-ion anisotropy of $D = 5.8 \text{ cm}^{-1}$ and anisotropic g -factors of $g_{\perp} = 4.50$ and $g_{\parallel} = 4.16$ (Fig. S9 [29]). However, to observe such a low-energy first excited Kramers doublet would require extremely high axial distortions (Fig. 8b), which would then require g -factors far from those obtained in simulations (Fig. 8a). Unsurprisingly, therefore, understanding the low-field data requires a model involving spin-spin exchange interactions.

The 11.6 cm^{-1} and 17.2 cm^{-1} spin gaps also cannot be explained using the phenomenological theory of antiferromagnetic resonance (AFMR) for collinear magnets with axial magnetic anisotropy [38]. The model predicts two excitation modes with spin-flop and spin-flip reorientations with increasing magnetic field. The magnetic field softens the AFMR resonance energies until the spin gaps close at the critical fields, which are directly related to the zero-field energies by the g -factor. But when we use the experimental spectroscopic g -factors, the calculated energies are significantly lower than the observed spin gaps, meaning the critical fields would need to be much higher than those observed in the magnetization data for the spin gaps to be AFMR modes. Again, a more involved spin-spin interaction model is needed to understand the spectroscopic data in the lower field regions.

D. Paramagnetic magnetization and susceptibility

For Li_2CoCl_4 , spin-orbit coupling is critical to understanding the susceptibility and magnetization, which are both influenced by the material's low-energy Kramers doublets. Fig. 10 compares the experimental data in the paramagnetic region to EASYSPIN calculations utilizing Eq. 1 for three cases: a spin- $\frac{1}{2}$ model with the spectroscopic anisotropic g -factors, a spin-orbit coupling model with the experimental spectroscopic parameters, and a spin-orbit coupling model with optimized spectroscopic parameters. All three models qualitatively match the shape of the magnetization data and indicate a saturated moment near $2\text{--}2.75 \mu_{\text{B}}$, but they differ significantly in describing the susceptibility data. While the spin-orbit coupling models reasonably match the low- and high-temperature slopes of the susceptibility, the spin- $\frac{1}{2}$ model only captures the low-temperature behavior. Improvements to the spin-orbit coupling model would need to consider higher-order spin-orbit interactions and electronic structure effects.

E. Evidence of XY-like interactions

Our calculations (Fig. 8b) estimate an energy gap between the two lowest doublets of 264 cm^{-1} (32.7 meV), indicating that Co^{2+} ions in Li_2CoCl_4 remain in the ground state Kramers doublet at low temperatures. This state can be mapped to an effective spin- $\frac{1}{2}$ state with an exchange interaction, JS_1S_2 , between next-neighbor spins exhibiting anisotropy of the type $\beta = J_z/J_x \neq 1$. Solving the spin-orbit Hamiltonian (Eq. 1) using spectroscopically determined parameters enables an estimation of the magnetic coupling anisotropy, yielding $\beta = 0.41$ for Li_2CoCl_4 (see the supplemental material for details [29]). This value of β classifies Li_2CoCl_4 as a system with easy-plane anisotropy, mirroring the g -factor anisotropy. Most Co-based chain materials, such as CsCoCl_3 [19], $\text{CoCl}_2 \cdot 2\text{H}_2\text{O}$ [39], CoNb_2O_6 [40], $[\text{Co}(\text{NCS})_2(4\text{-methoxypyridine})_2]_n$ [41], $\text{Co}(\text{N}_2\text{H}_5)_2(\text{SO}_4)_2$ [42], and $(\text{Ba,Sr})\text{Co}_2\text{V}_2\text{O}_8$ [43], exhibit Ising anisotropy ($\beta > 1$). We believe that the tetragonal distortion of the CoCl_6 octahedron in Li_2CoCl_4 , in contrast to the trigonal distortion in those systems, may serve as the underlying mechanism for XY anisotropy.

The neutron diffraction data is also compatible with ac -plane anisotropy. Though the magnetic intensity changes in the polycrystalline data support a reorientation along c , there were no observed reflections that violate a rotation through the a axis, and the refinement with moment components along a and c ($C2'/m'$ space group) was nearly identical to that with moments only along c . In contrast, the noted increase of the (020) reflection indicates that the magnetic moments are not rotating through the b axis. Previous DFT results using an experimental unit cell also indicate that moments along a or c are extremely similar energetically [18].

Qualitatively, the magnetic heat capacity of Li_2CoCl_4 at temperatures just above the long-range magnetic ordering [18] displays a hump similar to that of the predicted heat capacity for an isolated spin- $\frac{1}{2}$, XY chain with $J_x = J_y$, $J_z = 0$, and an applied field along the z direction [44]. Fitting the heat capacity of Cs_2CoCl_4 [45], a compound with tetrahedrally-coordinated Co^{2+} which also has a long-range ordering lambda peak and a hump in its magnetic heat capacity, to this model gives an intrachain exchange interaction parameter. However, we could not similarly fit the heat capacity of polycrystalline Li_2CoCl_4 , which has appreciable interchain interactions. Our neutron diffraction data suggest that the hump in the magnetic heat capacity stems from short range order due to the spin-flop transition.

V. CONCLUSIONS

Li_2CoCl_4 exhibits strongly anisotropic magnetic properties. Neutron diffraction suggests that the moments within the octahedrally coordinated chains of Co^{2+} pre-

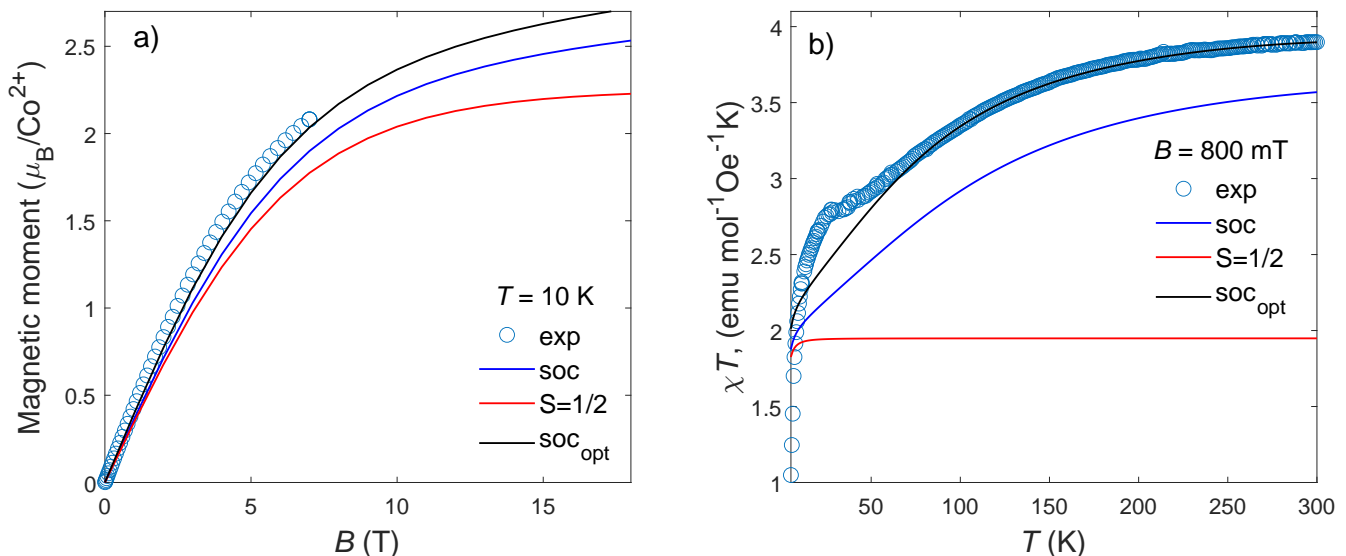


FIG. 10. Experimental (a) magnetization data at 10 K and (b) susceptibility data at 0.8 T on Li_2CoCl_4 powder (“exp”) are presented for a spin- $\frac{1}{2}$ model using $g_{\perp} = 5.23$ and $g_{\parallel} = 2.77$ (“S=1/2”); a spin-orbit coupling model using the spectroscopically determined parameters $\alpha = 1.77$, $\Delta = 2$, and $\lambda = 157 \text{ cm}^{-1}$ (“soc”); and a spin-orbit coupling model using the parameters $\alpha = 2$, $\Delta = 2.2$, and $\lambda = 110 \text{ cm}^{-1}$, adjusted to match the experimental data (“soc_{opt}”).

fer alignment along the crystallographic c axis, though an ac -plane canted moment could not be ruled out under applied magnetic fields. At zero field, the moments align ferromagnetically within the chains and antiferromagnetically between nearest-neighboring chains. At nonzero fields below 1.6 T, neutron diffraction shows that the antiferromagnetic structure is unchanged, but with increasing magnetic field, the anti-aligned chains undergo a spin-flop transition to a field-aligned ferromagnetic state, likely with $Cm'm'm$ symmetry. For the randomly oriented crystallites in a polycrystalline sample, a majority of the chains are aligned near 3.5 T. The chains do not transition to a ferrimagnetic state at intermediate fields as in $\text{CoCl}_2 \cdot 2\text{H}_2\text{O}$.

Anisotropic g -factors and magnetic spectroscopy data confirm a well-separated Kramers doublet ground state ($J = \frac{1}{2}$) for the Co^{2+} ion that is 32.7 meV below the first excited state. Consequently, Li_2CoCl_4 can be modeled as an effective spin- $\frac{1}{2}$ system of Co^{2+} chains with significant spin-orbit coupling and interchain interactions. The $J = \frac{1}{2}$ ground state and strong spin-orbit coupling explain the qualitative shape of magnetization and susceptibility data in the paramagnetic region, as well as the refined magnetic moment from neutron diffraction, the entropy recovery extracted from previous heat capacity data, and the difficulty in fitting the paramagnetic susceptibility to a purely Curie-Weiss shape. The tetragonal distortion of the CoCl_6 octahedra may also produce XY -like magnetic interactions, with a calculation of the interaction parameter ratio J_z/J_x yielding the value 0.41. XY anisotropy distinguishes Li_2CoCl_4 from other Co^{2+} chain magnets that have trigonally distorted octahedra

and display Ising-like anisotropy.

Further work should explore this anisotropy and its influence on the unexplained spin gaps below the moment saturation field by developing a model of spin-spin interactions between the cobalt ions. The models will be aided by single crystal neutron scattering experiments. Single crystal magnetization and neutron data along the three crystallographic axes would also improve the description of the magnetic behavior, allowing for a more precise determination of the moment saturation field and for an evaluation of potential magnetic moment canting within the ac plane. Overall, Li_2CoCl_4 offers a rare opportunity to study the combined effects of effective spin- $\frac{1}{2}$ behavior and XY -like magnetism on spin dynamics in an octahedrally coordinated Co^{2+} system.

ACKNOWLEDGMENTS

The authors acknowledge the use of facilities and instrumentation supported by NSF through the University of Illinois Materials Research Science and Engineering Center DMR-1720633. A portion of this research used resources at the High Flux Isotope Reactor, a DOE Office of Science User Facility operated by the Oak Ridge National Laboratory. The beam time was allocated to HB-2A (POWDER) on proposal number IPTS-30219. A portion of this work was performed at the National High Magnetic Field Laboratory, which is supported by National Science Foundation Cooperative Agreement No. DMR-2128556 and the State of Florida.

- [1] A. Vasiliev, O. Volkova, E. Zvereva, and M. Markina, Milestones of low-D quantum magnetism, *npj Quantum Materials* **3**, 18 (2018).
- [2] R. Coldea, D. A. Tennant, E. M. Wheeler, E. Wawrzynska, D. Prabhakaran, M. Telling, K. Habicht, P. Smeibidl, and K. Kiefer, Quantum criticality in an Ising chain: experimental evidence for emergent E8 symmetry, *Science* **327**, 177 (2010).
- [3] J. Larsen, T. K. Schäffer, U. B. Hansen, S. L. Holm, S. R. Ahl, R. Toft-Petersen, J. Taylor, G. Ehlers, J. Jensen, H. M. Rønnow, K. Lefmann, and N. B. Christensen, Spin excitations and quantum criticality in the quasi-one-dimensional Ising-like ferromagnet $\text{CoCl}_2 \cdot 2\text{D}_2\text{O}$ in a transverse field, *Physical Review B* **96**, 174424 (2017).
- [4] Z. Wang, T. Lorenz, D. I. Gorbunov, P. T. Cong, Y. Kohama, S. Niesen, O. Breunig, J. Engelmayr, A. Herman, J. Wu, *et al.*, Quantum criticality of an Ising-like spin- $\frac{1}{2}$ antiferromagnetic chain in a transverse magnetic field, *Physical Review Letters* **120**, 207205 (2018).
- [5] M. H. Karigerasi, L. K. Wagner, and D. P. Shoemaker, Uncovering anisotropic magnetic phases via fast dimensionality analysis, *Physical Review Materials* **2**, 094403 (2018).
- [6] R. Kanno, Y. Takeda, and O. Yamamoto, Ionic conductivity of solid lithium ion conductors with the spinel structure: Li_2MCl_4 ($M = \text{Mg}, \text{Mn}, \text{Fe}, \text{Cd}$), *Materials Research Bulletin* **16**, 999 (1981).
- [7] R. Kanno, Y. Takeda, K. Takada, and O. Yamamoto, Phase diagram and ionic conductivity of the lithium chloride-iron (II) chloride system, *Solid State Ionics* **9**, 153 (1983).
- [8] W. Schmidt and H. D. Lutz, Fast ionic conductivity and dielectric properties of the lithium halide spinels Li_2MnCl_4 , Li_2CdCl_4 , Li_2MnBr_4 , and Li_2CdBr_4 , *Berichte der Bunsengesellschaft für physikalische Chemie* **88**, 720 (1984).
- [9] R. Kanno, Y. Takeda, A. Takahashi, O. Yamamoto, R. Suyama, and S. Kume, New double chloride in the LiCl-CoCl_2 system: II. Preparation, crystal structure, phase transformation, and ionic conductivity of Li_2CoCl_4 spinel, *Journal of Solid State Chemistry* **71**, 196 (1987).
- [10] R. Kanno, Y. Takeda, and O. Yamamoto, Structure, ionic conductivity and phase transformation of double chloride spinels, *Solid State Ionics* **28**, 1276 (1988).
- [11] R. Kanno, Y. Takeda, A. Takahashi, O. Yamamoto, R. Suyama, and S. Kume, Structure, ionic conductivity, and phase transformation in new polymorphs of the double chloride spinel, Li_2FeCl_4 , *Journal of Solid State Chemistry* **72**, 363 (1988).
- [12] R. Kanno, Y. Takeda, A. Matsumoto, O. Yamamoto, R. Suyama, and S. Kume, Synthesis, structure, ionic conductivity, and phase transformation of new double chloride spinel, Li_2CrCl_4 , *Journal of Solid State Chemistry* **75**, 41 (1988).
- [13] H. D. Lutz, P. Kuske, and K. Wussow, Ionic motion of tetrahedrally and octahedrally coordinated lithium ions in ternary and quaternary halides, *Solid State Ionics* **28**, 1282 (1988).
- [14] K. Wussow, H. Haeuseler, P. Kuske, W. Schmidt, and H. D. Lutz, Lattice vibration spectra: XLVIII. Infrared and Raman studies of spinel-type fast ionic conductors Li_2MCl_4 ($M = \text{Mg}, \text{V}, \text{Cr}, \text{Mn}, \text{Fe}, \text{Co}, \text{Zn}, \text{Cd}$) and Li_2MnBr_4 , *Journal of Solid State Chemistry* **78**, 117 (1989).
- [15] H. D. Lutz, Schnelle lithium-ionenleiter-chemie und anwendung, *Nachrichten aus Chemie, Technik und Laboratorium* **43**, 418 (1995).
- [16] R. Kanno, Y. Takeda, K. Takada, and O. Yamamoto, Ionic conductivity and phase transition of the spinel system $\text{Li}_{2-2x}\text{M}_{1+x}\text{Cl}_4$ ($M = \text{Mg}, \text{Mn}, \text{Cd}$), *Journal of The Electrochemical Society* **131**, 469 (1984).
- [17] J. Cerisier, C. Guillot, P. Palvadeau, and M. Spiesser, Les conducteurs ioniques $\text{Li}_{1+x}\text{FeCl}_4$ Ière partie: Preparation-caracterisation, *Materials Research Bulletin* **21**, 575 (1986).
- [18] Z. W. Riedel, Z. Jiang, M. Avdeev, A. Schleife, and D. P. Shoemaker, Zero-field magnetic structure and metamagnetic phase transitions of the cobalt chain compound Li_2CoCl_4 , *Physical Review Materials* **7**, 104405 (2023).
- [19] N. Achiwa, Linear antiferromagnetic chains in hexagonal ABCl_3 -type compounds (A; Cs, or Rb, B; Cu, Ni, Co, or Fe), *Journal of the Physical Society of Japan* **27**, 561 (1969).
- [20] J. K. Kjems, J. Als-Nielsen, and H. Fogedby, Spin-wave dispersion in $\text{CoCl}_2 \cdot 2\text{D}_2\text{O}$: A system of weakly coupled Ising chains, *Physical Review B* **12**, 5190 (1975).
- [21] W. Montfrooij, G. E. Granroth, D. G. Mandrus, and S. E. Nagler, Spin dynamics of the quasi-one-dimensional ferromagnet $\text{CoCl}_2 \cdot 2\text{D}_2\text{O}$, *Physical Review B* **64**, 134426 (2001).
- [22] M. Mena, N. Hämmi, S. Ward, E. Hirtenlechner, R. Bewley, C. Hubig, U. Schollwöck, B. Normand, K. W. Krämer, D. F. McMorrow, and C. Rüegg, Thermal control of spin excitations in the coupled Ising-chain material RbCoCl_3 , *Physical Review Letters* **124**, 257201 (2020).
- [23] D. E. Cox, G. Shirane, B. C. Frazer, and A. Narath, Neutron diffraction determination of the intermediate-field magnetic structure of $\text{CoCl}_2 \cdot 2\text{H}_2\text{O}$, *Journal of Applied Physics* **37**, 1126 (1966).
- [24] H. Weitzel and W. Schneider, Neutron diffraction determination of the magnetic phases of $\text{CoCl}_2 \cdot 2\text{H}_2\text{O}$, *Solid State Communications* **14**, 1025 (1974).
- [25] B. H. Toby and R. B. Von Dreele, *GSAS - II*: the genesis of a modern open-source all purpose crystallography software package, *Journal of Applied Crystallography* **46**, 544 (2013).
- [26] J. M. Perez-Mato, S. V. Gallego, E. S. Tasci, L. Elcoro, G. de la Flor, and M. I. Aroyo, Symmetry-based computational tools for magnetic crystallography, *Annual Review of Materials Research* **45**, 217 (2015).
- [27] K. Momma and F. Izumi, *VESTA 3* for three-dimensional visualization of crystal, volumetric and morphology data, *Journal of Applied Crystallography* **44**, 1272 (2011).
- [28] S. Stoll and A. Schweiger, EasySpin, a comprehensive software package for spectral simulation and analysis in EPR, *Journal of Magnetic Resonance* **178**, 42 (2006).
- [29] See Supplemental Material at [URL will be inserted by publisher] for additional information, including Ref. [46].
- [30] T. Nagamiya, K. Yosida, and R. Kubo, Antiferromagnetism, *Advances in Physics* **4**, 1 (1955).
- [31] B. Hu, F. Geng, M. Shen, C. Zhao, Q. Qiu, Y. Lin,

- C. Chen, W. Wen, S. Zheng, X. Hu, *et al.*, A multifunctional manipulation to stabilize oxygen redox and phase transition in 4.6 V high-voltage LiCoO₂ with sXAS and EPR studies, *Journal of Power Sources* **516**, 230661 (2021).
- [32] B. Hu, F. Geng, M. Shen, and B. Hu, The study of electrochemical cycle for LiCoO₂ by dual-mode EPR, *Magnetic Resonance Letters* **3**, 61 (2023).
- [33] A. Abragam and M. H. L. Pryce, The theory of paramagnetic resonance in hydrated cobalt salts, *Proceedings of the Royal Society of London. Series A. Mathematical and Physical Sciences* **206**, 173 (1951).
- [34] M. E. Lines, Magnetic properties of CoCl₂ and NiCl₂, *Physical Review* **131**, 546 (1963).
- [35] O. Kahn, *Molecular Magnetism* (Wiley-VCH, Weinheim, 1993).
- [36] H. Shiba, Y. Ueda, K. Okunishi, S. Kimura, and K. Kindo, Exchange interaction via crystal-field excited states and its importance in CsCoCl₃, *Journal of the Physical Society of Japan* **72**, 2326 (2003).
- [37] F. Lloret, M. Julve, J. Cano, R. Ruiz-García, and E. Pardo, Magnetic properties of six-coordinated high-spin cobalt (II) complexes: Theoretical background and its application, *Inorganica Chimica Acta* **361**, 3432 (2008).
- [38] V. N. Glazkov, A. I. Smirnov, A. Revcolevschi, and G. Dhalle, Magnetic resonance study of the spin-reorientation transitions in the quasi-one-dimensional antiferromagnet BaCu₂Si₂O₇, *Physical Review B* **72**, 104401 (2005).
- [39] U. Hansen, O. F. Syljuasen, J. Jensen, T. Schaffer, C. Andersen, M. Boehm, J. A. Rodriguez-Rivera, N. B. Christensen, and K. Lefmann, Magnetic Bloch oscillations and domain wall dynamics in a near-Ising ferromagnetic chain, *Nature Communications* **13**, 2547 (2022).
- [40] K. Amelin, J. Engelmayer, J. Viirik, U. Nagel, T. Rööm, T. Lorenz, and Z. Wang, Experimental observation of quantum many-body excitations of E8 symmetry in the Ising chain ferromagnet CoNb₂O₆, *Physical Review B* **102**, 104431 (2020).
- [41] M. Rams, A. Jochim, M. Böhme, T. Lohmiller, M. Ceglarska, M. M. Rams, A. Schnegg, W. Plass, and C. Näther, Single-chain magnet based on cobalt (II) thiocyanate as XXZ spin chain, *Chemistry—A European Journal* **26**, 2837 (2020).
- [42] S. Calder, L. D. Sanjeeva, V. O. Garlea, J. Xing, R. J. Terry, and J. W. Kolis, Magnetic interactions in the one-dimensional spin-chain metal-organic compounds *M*(N₂H₅)₂(SO₄)₂ (*M*=Cu, Co, Mn), *Physical Review Materials* **6**, 124407 (2022).
- [43] J. Yang, X. Wang, and J. Wu, Magnetic excitations in the one-dimensional Heisenberg-Ising model with external fields and their experimental realizations, *Journal of Physics A: Mathematical and Theoretical* **56**, 013001 (2023).
- [44] S. Katsura, Statistical mechanics of the anisotropic linear Heisenberg model, *Physical Review* **127**, 1508 (1962).
- [45] H. A. Algra, L. J. De Jongh, H. W. J. Blöte, W. J. Huiskamp, and R. L. Carlin, Heat capacity of Cs₂CoCl₄ below 1 K, compared with the $S=\frac{1}{2}$ linear chain *XY* model, *Physica B+C* **82**, 239 (1976).
- [46] T. Oguchi, Theory of magnetism in CoCl₂·2H₂O, *Journal of the Physical Society of Japan* **20**, 2236 (1965).

Applied-field magnetic structure and spectroscopy shifts of the effective spin- $\frac{1}{2}$, XY -like magnet Li_2CoCl_4

Supplemental Material

Zachary W. Riedel, Mykhaylo Ozerov, Stuart Calder, and Daniel P. Shoemaker

1 Additional diffraction data and refinements

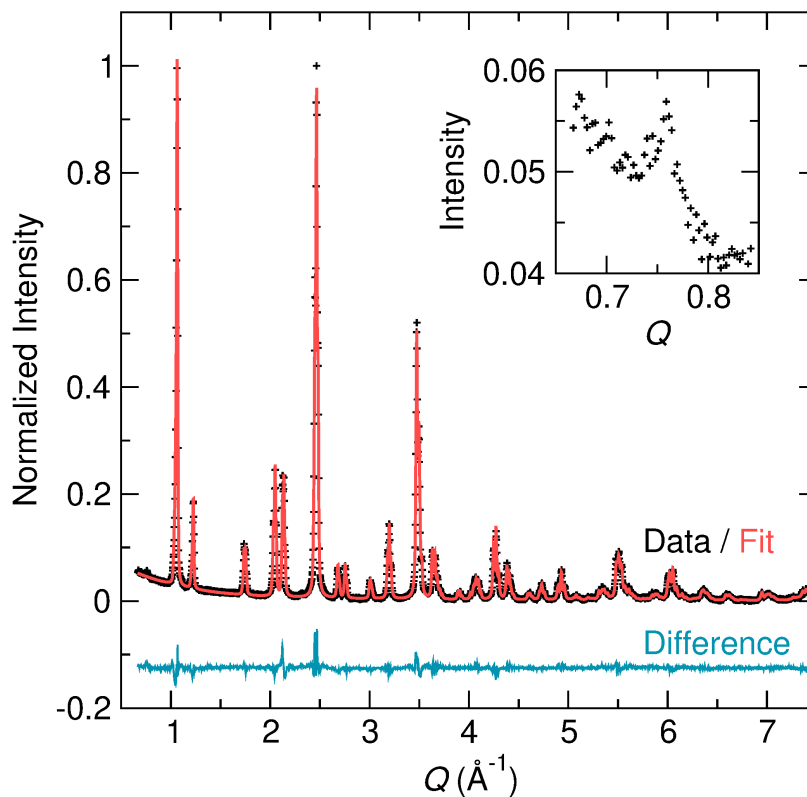


Figure S1: We exposed a portion of the sample used for the neutron powder diffraction experiments to air for 15–30 s before sealing it under vacuum and collecting powder X-ray diffraction data with a Mo- $K\alpha$ source. The data refines well to the known structure, but a low intensity reflection at 0.77 \AA^{-1} appears (see inset). Though this peak also appears in the neutron powder diffraction data, where care was taken to avoid any air exposure, its intensity does not change and is low relative to the reflections from the nuclear and magnetic cells of Li_2CoCl_4 .

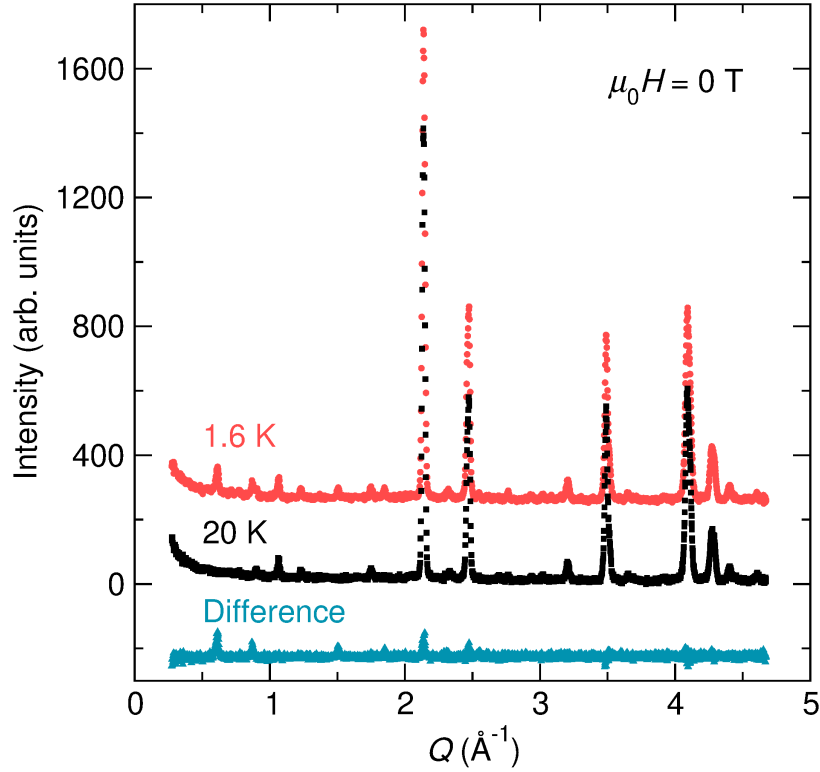


Figure S2: Zero-field neutron powder diffraction data collected at 20 K and 1.6 K are compared, showing the emergence of antiferromagnetic ordering that breaks the nuclear cell's C -centering, allowing reflections where $h + k \neq 2n$.

Table S1: Rietveld refinement results for base temperature, constant magnetic field scans with a constrained moment of $2.10 \mu_B$ are listed. R_w values are included to compare the constrained moment fits to the unconstrained/refined moment fits tabulated in the main text. Scans below 1.6 T only include the antiferromagnetic P_Cbam phase, while those above 1.6 T also include the ferromagnetic $Cm'm'm$ phase.

Field (T)	Magnetic Phase (% P_Cbam - % $Cm'm'm$)	R_w (%)	Refined Moment R_w (%)
0	100 - 0	5.995	5.995
0.8	100 - 0	5.836	5.825
1.5	100 - 0	5.964	5.931
2.5	55(2) - 45(2)	6.062	5.971
3.5	35(2) - 65(2)	6.007	5.964
4.5	17(2) - 83(2)	5.722	5.721
5.5	11(2) - 89(2)	5.703	5.702

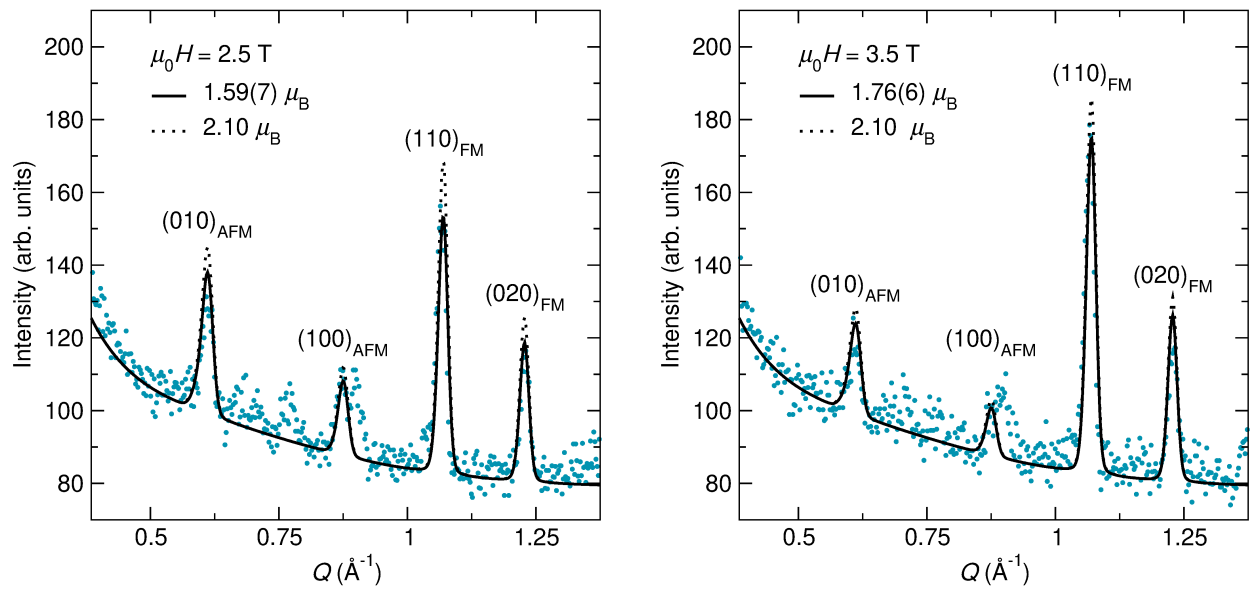


Figure S3: Because of the intermediate-field, spin-flop transition, the difference between refining the magnetic moment or constraining it to the zero-field value of $2.10 \mu_B$ is most prominent for the highest intensity antiferromagnetic (“AFM”) and ferromagnetic/nuclear (“FM”) peaks in the 2.5 and 3.5 T data. For the 0, 0.8, 1.5, 4.5, and 5.5 T refinements, the difference is negligible. Unfit peaks are background/impurity peaks noted in the main text.

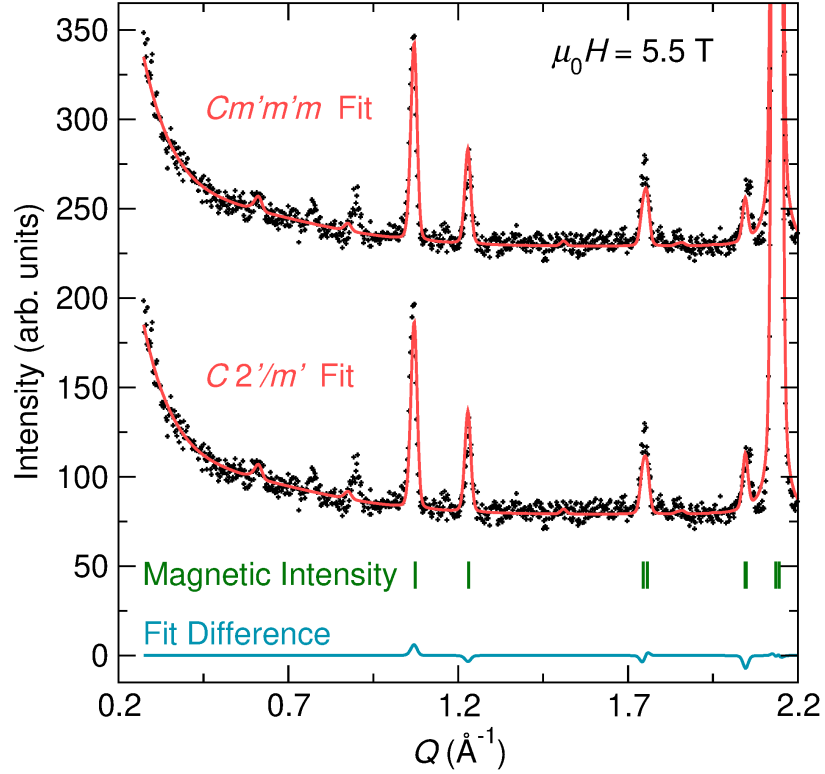


Figure S4: At 5.5 T, the diffraction data can be fit with a small fraction of the antiferromagnetic phase plus a majority ferromagnetic phase with either $Cm'm'm$ symmetry (moment component along c) or $C2'/m'$ symmetry (moment components along a and c). The difference between the fits ($Cm'm'm$ fit – $C2'/m'$ fit) shows minor changes. Both space groups have the same reflection conditions as the nuclear cell; the peak positions are marked with ticks. Unfit peaks are background/impurity peaks discussed in the main text.

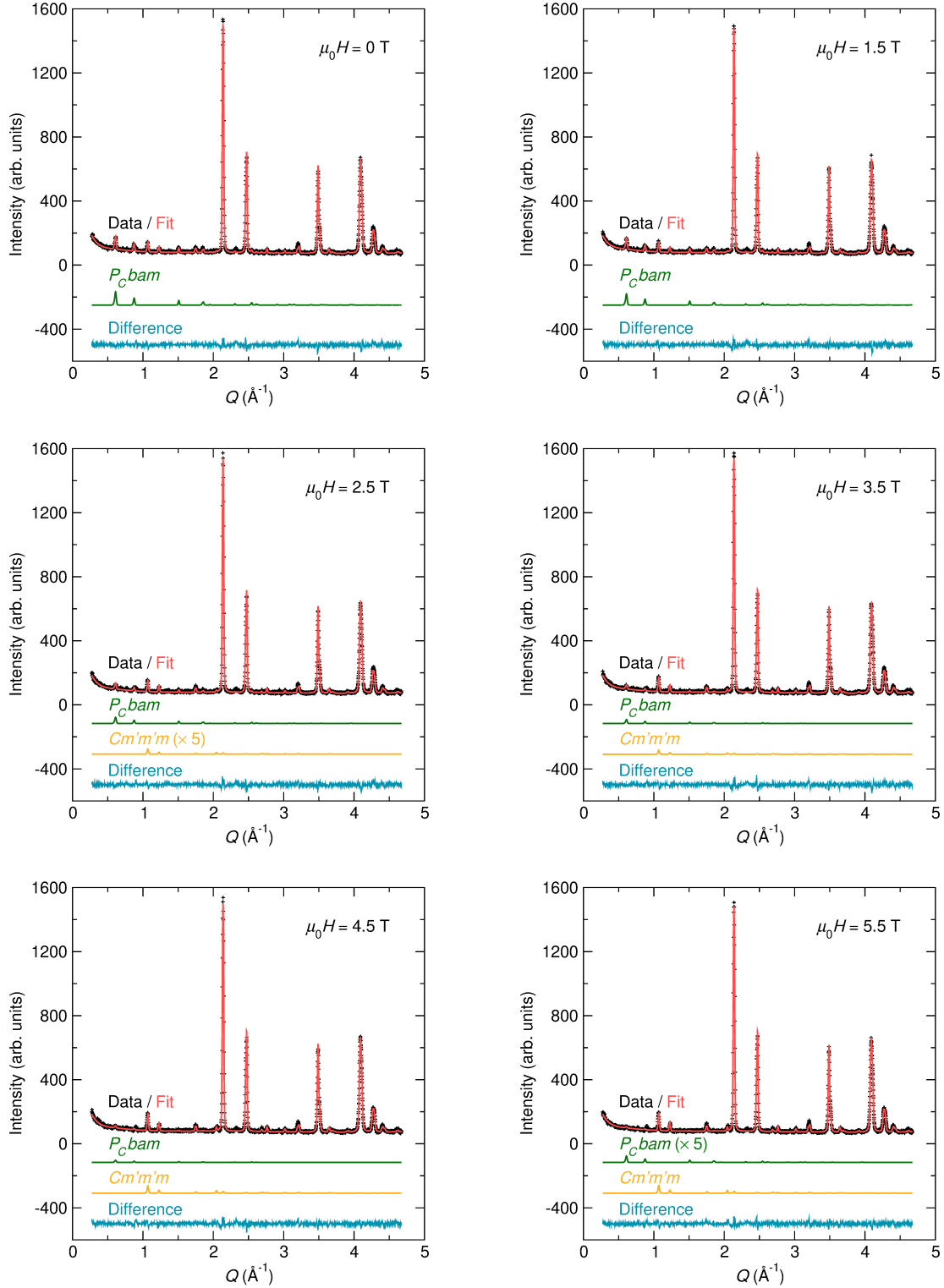


Figure S5: Neutron powder diffraction refinements not in the main text are shown along with full pattern refinements of the 2.5 and 5.5 T data. At 0 and 1.5 T, we observe only antiferromagnetic reflections ($P_C bam$). At higher fields, the ferromagnetic phase ($Cm'm'm$) co-exists with the antiferromagnetic one.

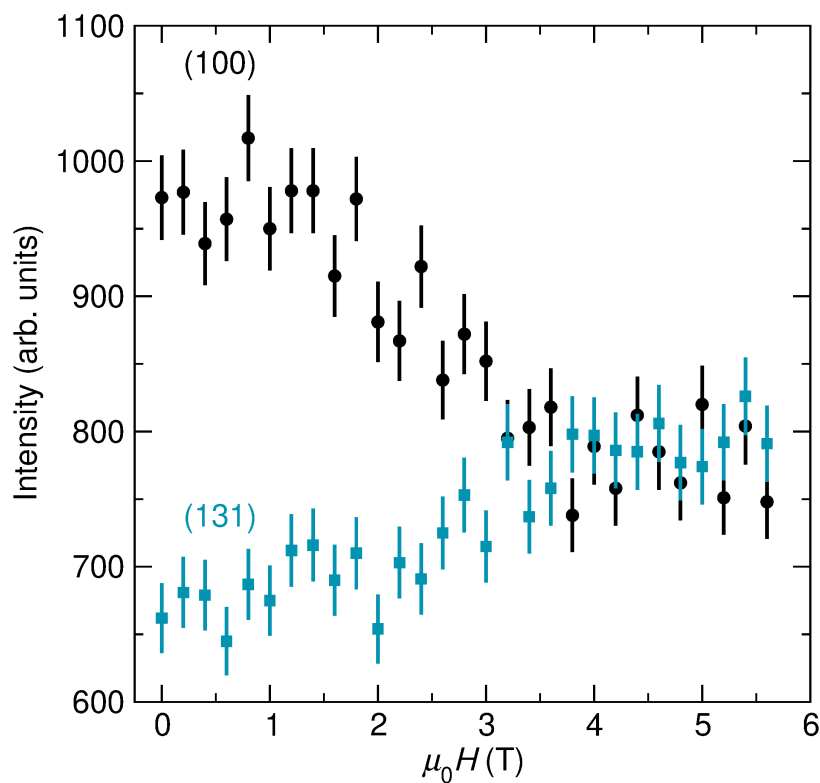


Figure S6: While collecting a magnetic field sweep of the prominent (010) antiferromagnetic reflection, other detectors captured information about the (100) antiferromagnetic reflection and the (131) nuclear/ferromagnetic reflection. Neither detector was centered on the (100) or (131) peak's maximum, but both captured the trend toward moments aligned between Co^{2+} chains with increasing field. The convergence of both peaks to similar intensities is a coincidence of the higher background intensity around the (100) peak and the relatively low intensity of the (131) peak.

2 High-field magnetic susceptibility data

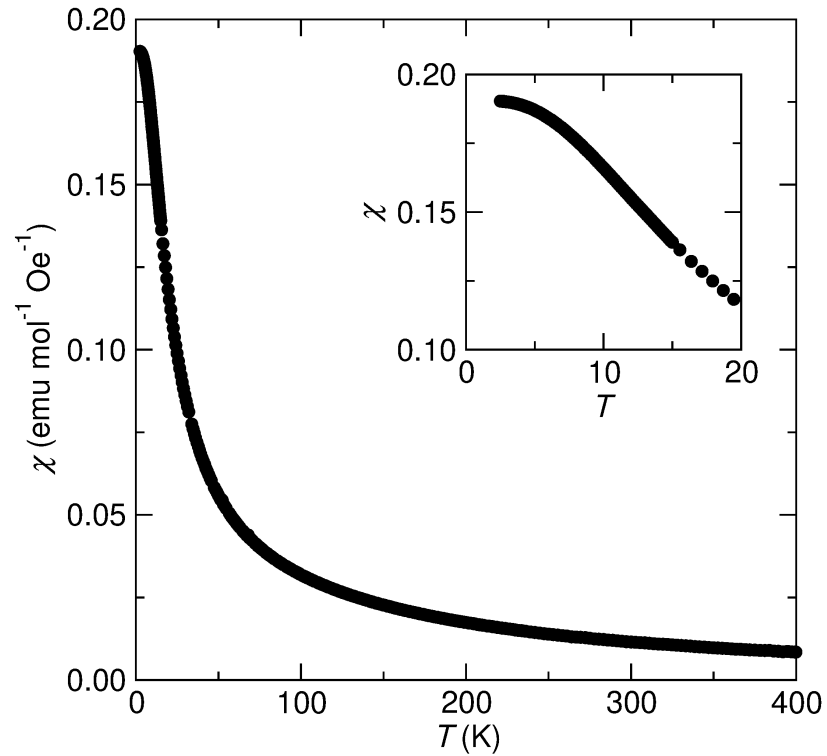


Figure S7: The zero-field cooled (ZFC) magnetic susceptibility of Li_2CoCl_4 was measured at 70 kOe from 2.5 to 400 K in a Quantum Design Magnetic Property Measurement System (MPMS3), using the direct current measurement mode. While the susceptibility levels off near the base temperature (inset), no sharp rise associated with purely ferromagnetic order is observed and no cusp associated with long-range antiferromagnetic order is observed.

3 Additional IR data

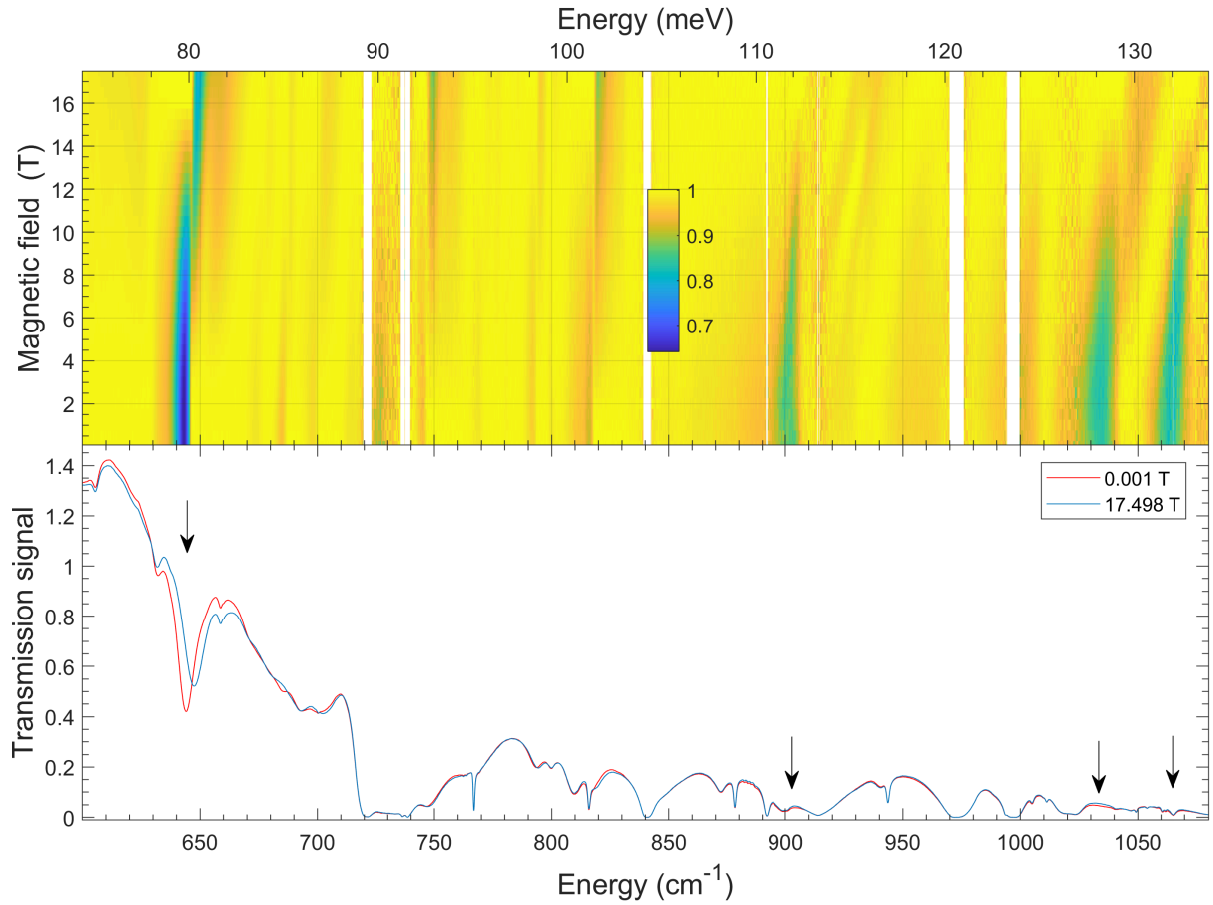


Figure S8: (top) Heatmap of the normalized transmittance, where the color represents relative changes in the (bottom) powder transmission signal induced by the magnetic field. The decrease in transmission at high frequencies due to spectrometer settings makes it difficult to distinguish between the 0 and 17.5 T spectra. Instead, normalizing all spectra to the reference spectrum highlights the relevant field-induced changes. The arrows indicate the zero-field positions of the most intense spectral features, which we attribute to transitions between Kramers doublets of the orbital ${}^4T_{1g}$ state.

4 Simulation of IR data with free-ion models

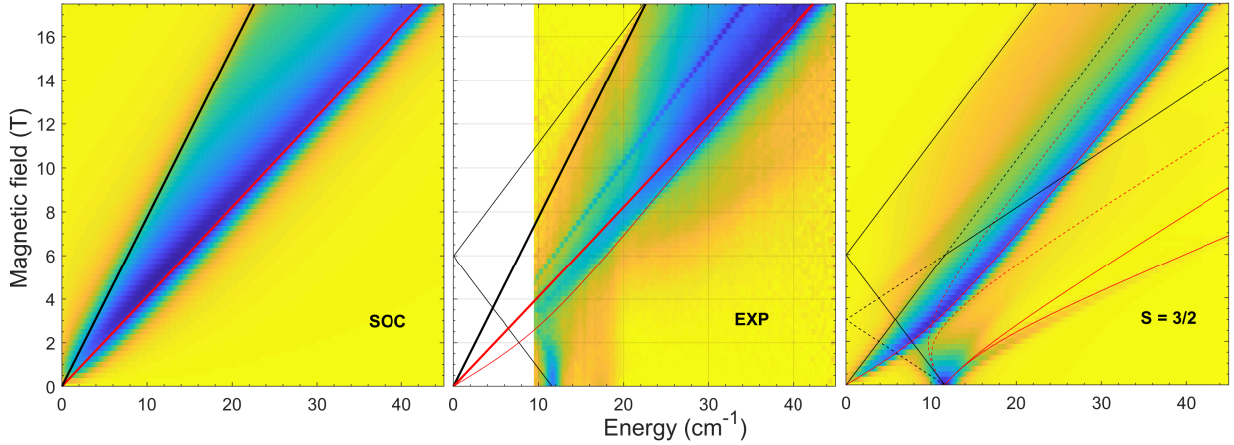


Figure S9: Comparison of the experimental magnetic resonance absorption heatmap (middle) with simulation results obtained using Hamiltonians for the free-ion approximation with spin-orbit coupling (left) and spin- $\frac{3}{2}$ (right) models for a powder sample using the EASYSPIN package [1]. The parameters of the Hamiltonian are given in Table S2. The solid and dashed lines present the resonance excitations from the ground and first excited states respectively. The colored lines restrict the area of all possible magnetic resonances in polycrystalline samples, corresponding to the resonance dependence for magnetic field applied along g_{\parallel} (black) and g_{\perp} (red). The broadening shown is the best match to the 17.5 T experimental data.

Table S2: Spin Hamiltonian parameters used to simulate the magnetic resonance absorption spectra shown in Fig. S9.

Model	g_{\perp}	g_{\parallel}	$[D, E]$	$[\alpha, \lambda, \Delta/(\lambda\alpha)]$
SOC	2	2	—	1.77, 157, 2
$S = \frac{3}{2}$	4.5	4.16	5.8, 0	—

5 Evaluation of the exchange interaction anisotropy for an effective Heisenberg Hamiltonian model

Following Abragam and Pryce [2], the wavefunction of the ground state doublet for the spin-orbit Hamiltonian (Eq.1 in main text) is expressed with orbital-spin wavefunctions $|L, S\rangle$ as

$$\left| \pm \frac{1}{2} \right\rangle = a \left| \mp 1, \pm \frac{3}{2} \right\rangle + b \left| 0, \pm \frac{1}{2} \right\rangle + c \left| \pm 1, \mp \frac{1}{2} \right\rangle \quad (1)$$

where a , b , and c are coefficients dependent on $\Delta/(\lambda\alpha)$. If we use the spectroscopically estimated Δ , α , and λ parameters (listed in the main text and in Table S2), we find

$$a = -0.4931; b = 0.7844; c = -0.3763 \quad (2)$$

When the ground state is well separated from the first excited state, the total spin $S_{\text{tot}} = \frac{3}{2}$ within the ground state doublet can be described by a $S = \frac{1}{2}$ function

$$S_{\text{tot}}^{x,y} = qS^{x,y}, S_{\text{tot}}^z = pS^z \quad (3)$$

where q and p are coefficients defined as in Ref. [3].

$$\begin{aligned} p &= 3a^2 + b^2 - c^2 = 1.2032 \\ q &= 2b^2 + 2\sqrt{3}ac = 1.8733 \end{aligned} \quad (4)$$

Hence, the isotropic superexchange mechanism for neighboring total spins will be mapped to an effective $S = \frac{1}{2}$ Hamiltonian with an anisotropic exchange interaction

$$H_{XXZ} = J \sum_{i=1}^N (S_i^x S_{i+1}^x + S_i^y S_{i+1}^y + \beta S_i^z S_{i+1}^z) \quad (5)$$

where

$$\beta = \frac{p^2}{q^2} = 0.4125 \quad (6)$$

This approach for estimating the exchange anisotropy has previously been applied for the CsCoCl₃ quasi-1D Ising system [4, 5]. A comparison is shown in Fig. S10. Note that the energy and axial distortion of our calculations were multiplied by a factor of 1.5 to make our results compatible with Fig. 1 and Fig. 3 in ref. [5]. The factor of 1.5 is a coefficient in front of spin-orbit coupling term in the Hamiltonian used in Refs. [4, 5].

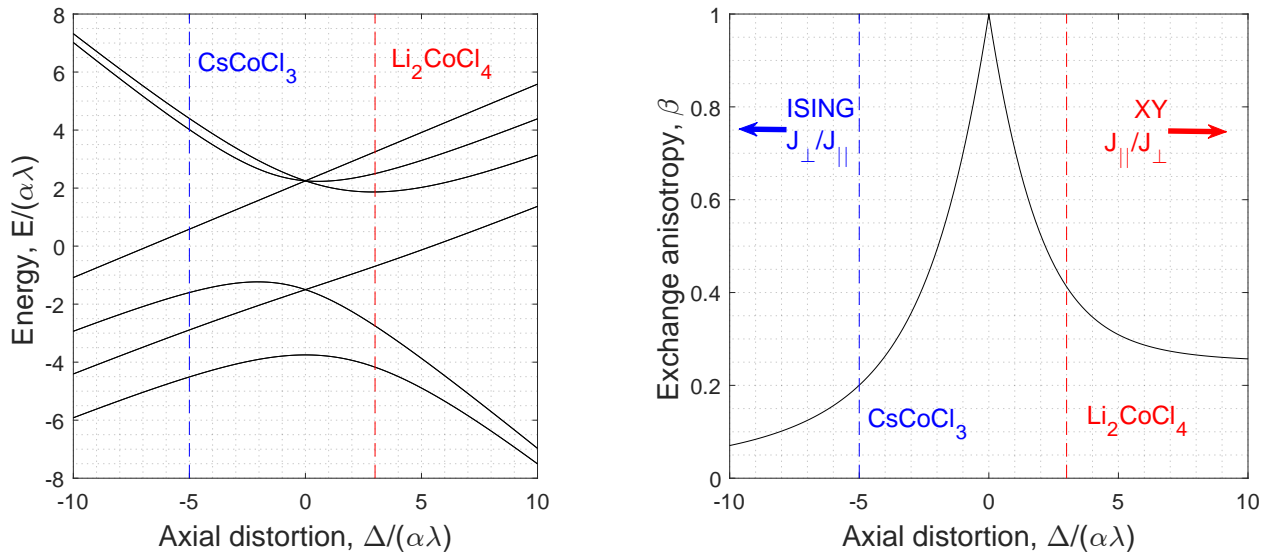


Figure S10: (left) Energy level splitting of the orbital triplet ground state of the Co^{2+} ion (${}^4T_{1g}$) due to axial distortion. (right) Ratio of the parallel and perpendicular components of the nearest-neighbor exchange interaction for a $S=\frac{1}{2}$ single-chain effective Hamiltonian. Dashed lines show the estimated distortion values for Li_2CoCl_4 (this work) and CsCoCl_3 [4].

References

- [1] S. Stoll and A. Schweiger, *Journal of Magnetic Resonance* **178**, 42 (2006).
- [2] A. Abragam and M. H. L. Pryce, *Proceedings of the Royal Society of London. Series A. Mathematical and Physical Sciences* **206**, 173 (1951).
- [3] T. Oguchi, *Journal of the Physical Society of Japan* **20**, 2236 (1965).
- [4] N. Achiwa, *Journal of the Physical Society of Japan* **27**, 561 (1969).
- [5] H. Shiba, Y. Ueda, K. Okunishi, S. Kimura, and K. Kindo, *Journal of the Physical Society of Japan* **72**, 2326 (2003).